

Article

Generation Mechanism of the Defects in g-C₃N₄ Synthesized in N₂ Atmosphere and the Method for Improving Photocatalysis Activity

Xinye Chang ¹, Huiqing Fan ^{1,*} , Lin Lei ¹, Xiaobo Wu ¹ , Weijia Wang ^{1,*} and Longtao Ma ^{2,*} 

¹ State Key Laboratory of Solidification Processing, School of Materials Science and Engineering, Northwestern Polytechnical University, Xi'an 710072, China

² Institute of Flexible Electronics, Northwestern Polytechnical University, Xi'an 710072, China

* Correspondence: hqfan@nwpu.edu.cn (H.F.); weijia.wang@nwpu.edu.cn (W.W.); iamltma@nwpu.edu.cn (L.M.)

Abstract: One of the most important methods for modifying semiconductors is defect engineering, but only the right quantity of defects in the right chemical environment can produce desirable results. Heat treatment processes associated with g-C₃N₄ are occasionally carried out in N₂ atmosphere, however, the catalytic performance of g-C₃N₄ produced by direct condensation of only nitrogen-rich precursors in N₂ atmosphere is often unsatisfactory. This is typically attributed to the introduction of numerous defects, but the actual relationship between the formation of defects and the N₂ atmosphere is rarely explained, and the resulting quantity of defects is difficult to control. We propose that the melam to melem transition is restricted due to the lack of O₂ during the heat treatment of the nitrogen-rich precursor of g-C₃N₄ in N₂ atmosphere, which leads to a substantial quantity of defects in the synthesized g-C₃N₄. To enhance its photocatalytic property, we propose a method to reduce the quantity of defects due to calcinating in N₂ atmosphere by protonating the precursor in a way that increases the polymerization of the product. The test analysis indicated that only a moderate quantity of defects that contribute to electron excitation and enhance the separation efficiency and density of photogenerated carriers were retained, and the hydrogen evolution performance of the prepared catalyst was significantly improved.

Keywords: photocatalysis; g-C₃N₄; defect engineering; N₂ atmosphere; protonation



Citation: Chang, X.; Fan, H.; Lei, L.; Wu, X.; Wang, W.; Ma, L. Generation Mechanism of the Defects in g-C₃N₄ Synthesized in N₂ Atmosphere and the Method for Improving Photocatalysis Activity. *Catalysts* **2023**, *13*, 269. <https://doi.org/10.3390/catal13020269>

Academic Editor: Wenjian Fang

Received: 24 December 2022

Revised: 22 January 2023

Accepted: 23 January 2023

Published: 25 January 2023



Copyright: © 2023 by the authors. Licensee MDPI, Basel, Switzerland. This article is an open access article distributed under the terms and conditions of the Creative Commons Attribution (CC BY) license (<https://creativecommons.org/licenses/by/4.0/>).

1. Introduction

Hydrogen is a type of secondary energy that has a plentiful supply, is environmentally friendly (no carbon emissions), and has a wide range of applications, which is gradually becoming one of the important carriers of the global energy transition [1]. However, the current main industrial hydrogen evolution methods, such as from fossil fuels, industrial by-products, and water through electrolysis, have more or less environmental pollution or high-cost problems, so the use of solar energy for photolytic water hydrogen evolution has become the most ideal way. Graphite carbon nitride (g-C₃N₄) as a nonmetallic semiconductor is considered one of the ideal candidates for hydrogen evolution from photolyzed water because it has a suitable energy band gap to satisfy the thermodynamic standards of photolyzed water and is easy to prepare and modify [2,3]. The direction of modification g-C₃N₄ usually focuses on facilitating the separation of photogenerated electron-hole pairs and increasing the specific surface area so that more photogenerated carriers can migrate to the surface-active sites to participate in redox reactions [4–6].

To enhance the separation of photogenerated carriers, it is necessary to adjust the chemical and electronic structure of g-C₃N₄, and one of the simplest and most efficient techniques is the introduction of defects [7–9]. However, only the right quantity of defects in the right chemical environment can produce desirable results [10,11]. Many unfavorable

defects will not only reduce or even inactivate the intrinsic photocatalytic ability of g-C₃N₄, but also hinder the migration of carriers and reduce its electrical conductivity [12]. The most common means to induce defects is doping, but many dopants are costly, contain heavy elements, or produce toxic gases/by-products during the subsequent calcination, which is contrary to the original intention of preparing a non-polluting photocatalyst, so we hope to construct self-generated defects. As the most common atmosphere, N₂ has been often used during the heat treatment of g-C₃N₄ [13–15]. However, compared to g-C₃N₄ prepared in air, the catalytic performance of g-C₃N₄ produced by direct condensation of just nitrogen-rich precursor in N₂ atmosphere tends to decrease in different degrees, which is usually attributed to the formation of defects. However, the actual relationship between the formation of defects and the N₂ atmosphere is rarely explained, and the resulting quantity of defects is difficult to control. Although other atmospheres such as H₂ or direct thermal etching in air can also introduce defects in g-C₃N₄, these conditions also remove many fragments that are only partially condensed, resulting in a lower yield of the finished product [16], in contrast to N₂ as a protective gas, which has no such concerns. In addition, the quantity of defects induced in H₂ atmosphere is also difficult to control [12], so this paper focuses on the defects of g-C₃N₄ induced by N₂ atmosphere.

Because g-C₃N₄ has a lamellar structure, interlayer exfoliation is an effective method to increase its specific surface area and catalytic activity point. Commonly used exfoliation methods include ultrasonic processing, ion intercalation, and heat treatment [17–19]. Interestingly, a similar effect can be achieved by utilizing the thermal triggering in-situ gas shock process. By applying this principle, Gao et al. [20] created ultrathin porous g-C₃N₄ using endogenous gas (CO₂, H₂O, and NH₃) from urea solution with an outstanding specific surface area of 190 m²·g⁻¹. Another method that can also generate a large amount of endogenous gas during the thermal polymerization process and ultimately obtain a large specific surface area is protonated pretreatment precursor. The process known as protonation is adding a proton (H⁺) to an atom, molecule, or ion. Zhong et al. [21] prepared porous g-C₃N₄ with improved polymerization and specific surface area by calcinating protonated melamine. After the protonation of melamine, the amino groups (-NH₂) at the end of the triazine units combine with the H⁺ to form -NH₃⁺ groups due to the large electronegativity and the presence of lone pair electrons, where the adsorbed H⁺ can facilitate the polymerization reaction, promote the release of NH₃ gas, and increase the polymerization of g-C₃N₄. Other reports have revealed that in addition to protonation, the -NH₂ groups of melamine can be partially oxidized to -OH and -COOH groups in a highly acidic environment, and these groups will generate H₂O and CO₂ gas in the subsequent polymerization reaction [22,23]. Due to a large amount of endogenous gas, g-C₃N₄ formed from the protonated precursor tends to exhibit a porous, thin, sheet-like shape.

In previous reports, the authors tended to introduce a moderate quantity of defects to improve the catalytic performance. In contrast, the present work reduces the quantity of defects in g-C₃N₄ synthesized in N₂ atmosphere that is detrimental to the catalytic reaction by increasing the degree of polymerization using the method of protonation pretreatment of precursor. Combined with the in-situ gas shock of extra endogenous gas, g-C₃N₄ with a large specific surface area, and a small quantity of high-quality defects was finally prepared. Furthermore, this work offers a methodical analysis of the mechanism underlying a large quantity of defects in the synthesized g-C₃N₄ caused by N₂ atmosphere. This work not only provides a fresh perspective on how to introduce the right quantity of defects, but also provides a deeper opinion on the intrinsic mechanism of defects formation in N₂ atmosphere.

2. Materials and Methods

2.1. Synthesis of HN-CN

Since every reagent was of analytical grade, no additional purification was necessary. In a typical synthesis, 3 g of melamine were dissolved into 30 mL of ethylene glycol solution (analytical reagent), followed by 30 mL of 65% nitric acid solution added drop by drop

and stirred for 8 h at room temperature. After stirring, the white precipitate was obtained by centrifugal washing with ethanol three times. The protonated melamine precursor (H-Me) was obtained by drying the collected precipitate for 8 h at 60 °C in a vacuum drying oven. Subsequently, the H-Me was transferred into a covered ceramic crucible and heated to 550 °C in an N₂ atmosphere at 5 °C/min and held for 2 h. After cooling to room temperature in the furnace, the product was ground to a powder in an agate mortar, and then, a high polymerization g-C₃N₄ with a moderate quantity of defects was obtained (noted as HN-CN).

2.2. Synthesis of CN, N-CN, and H-CN

In order to investigate the effect of heat treatment in the N₂ atmosphere and protonated precursor on the synthesized g-C₃N₄ separately, three control groups were prepared as follows:

(1) The 3 g of melamine was placed directly into a covered ceramic crucible, heated in air atmosphere with the same temperature gradient. After cooling and thorough grinding, the pristine g-C₃N₄ was obtained (noted as CN).

(2) The 3 g melamine was placed directly into a covered ceramic crucible and heated in the N₂ atmosphere with the same heat treatment conditions. After cooling and thorough grinding, the g-C₃N₄ containing a large quantity of defects was obtained (noted as N-CN).

(3) The same mass of H-Me was transferred in a covered ceramic crucible and heated in the air atmosphere with the same temperature gradient. After cooling and thorough grinding, the high polymerization g-C₃N₄ was obtained (noted as H-CN).

2.3. Characterization

X-ray diffractometer (XRD, 7000, Shimadzu, Kyoto, Japan) was used to analyze the lattice structure operated at 40 kV and 35 mA using Cu K α radiation ($\lambda = 1.5418 \text{ \AA}$). The chemical structure of the samples was analyzed using Fourier-transform infrared spectroscopy (FTIR, TENSOR27, Bruker, Billerica, MA, USA) with a diamond indenter. The chemical states of the samples were analyzed using X-ray photoelectron spectroscopy (XPS, Axis Supra, Kratos, Manchester, UK) with the Al K α radiation. A scanning electron microscope (SEM, Clara GMH, Tescan) and a field emission transmission electron microscope (TEM, Talos F200X, FEI, Hillsborough, USA) were used to investigate the surface morphologies. The elemental composition was examined using an energy dispersive X-ray spectrometer (EDS) mounted on the TEM. The nitrogen adsorption–desorption (Micromeritics 2460) method was used to examine the specific surface area and pore size at 77 K, where the specific surface area was determined using the Brunauer-Emmett-Teller method and the pore size distribution was calculated using the Barrett-Joyner-Halenda method. A spectrophotometer (Lambda 1050+) with BaSO₄ as reference was used to acquire the UV-vis diffuse reflectance spectra (DRS). A fluorescence spectrophotometer (FLS980, Edinburgh Instruments, Edinburgh, Britain, $\lambda = 325 \text{ nm}$) was used to investigate the photoluminescence (PL) characteristics. The electron paramagnetic resonance spectra (EPR, X-band Bruker A300, Karlsruhe, Germany) were used to characterize the paramagnetic characteristics at room temperature. Elemental analysis of samples using an element analyzer (EA, Elementar UNICUBE, Germany)

2.4. Electrochemical Test

All electrochemical tests in this research were carried out in a three-electrode system utilizing an electrochemical workstation (CHI660E, Shanghai Chenhua, Shanghai, China), using a 10 × 10 mm² Pt plate and an Ag/AgCl electrode as the counter and reference electrode, respectively. The working electrode was an 8 × 8 mm² indium tin oxide (ITO) conductive glass coated with prepared samples, and the electrolyte was 0.5 M Na₂SO₄ aqueous solution.

2.5. Photocatalytic Hydrogen Evolution Test

In a photocatalytic H₂ generation system (Beijing Perfectlight, Labsolar 6A, Beijing, China), investigations on photocatalytic H₂ evolution were carried out. Typically, the 100 mL solution containing 10 vol% triethanolamine (TEOA) was mixed with 50 mg of the prepared photocatalyst. Using H₂PtCl₆·6H₂O as a Pt source, 1 wt.% of Pt was in-situ deposited on the photocatalyst by photoreduction. A cooling water recirculation system maintained the reaction solution's temperature at 6 °C. The solution was then degassed and exposed to irradiation, and the quantity of evolved gas was measured using the gas chromatograph instrument (GC9808; Linghua, Shanghai, China) with a thermal conductivity detector. A 300W Xe lamp (PLS-SXE300; Perfectlight, Beijing, China) was used to provide irradiation conditions from the top of the reactor. A cutoff filter with a wavelength of >420 nm was applied to obtain visible light, and a succession of band-pass filters with wavelengths of 380, 420, 450, 500, and 550 nm were applied to get monochromatic light.

3. Results and Discussion

3.1. Characterization of Structure and Morphology

Melamine was chosen as the precursor of g-C₃N₄ because it possesses a triazine ring, which can minimize the effect of N₂ atmosphere on the π -conjugated structure to obtain a more complete heptazine-based framework structure. Additionally, nitric acid not only protonates the -NH₂ groups of melamine, but also allows the melamine molecules to self-assemble into rods and precipitate out, which facilitates the formation of a larger specific surface area after polymerization [21]. Figure 1 shows the schematic diagram of the synthesis of HN-CN. The weights of the final prepared CN, N-CN, H-CN, and HN-CN were 1.456 g, 1.875 g, 0.192 g, and 0.305 g, respectively (Figure S1a–d). Combined with Figure S1e, it can be seen that although the protonation of the precursor can enhance the specific surface area and polymerization of the product, it can also seriously reduce the yield. The increase in volume and weight of N-CN compared to CN and that of HN-CN compared to H-CN visually reflects the positive effect of heat treatment in N₂ atmosphere for increasing the product yield, which is one of the reasons for using N₂ atmosphere to introduce defects.

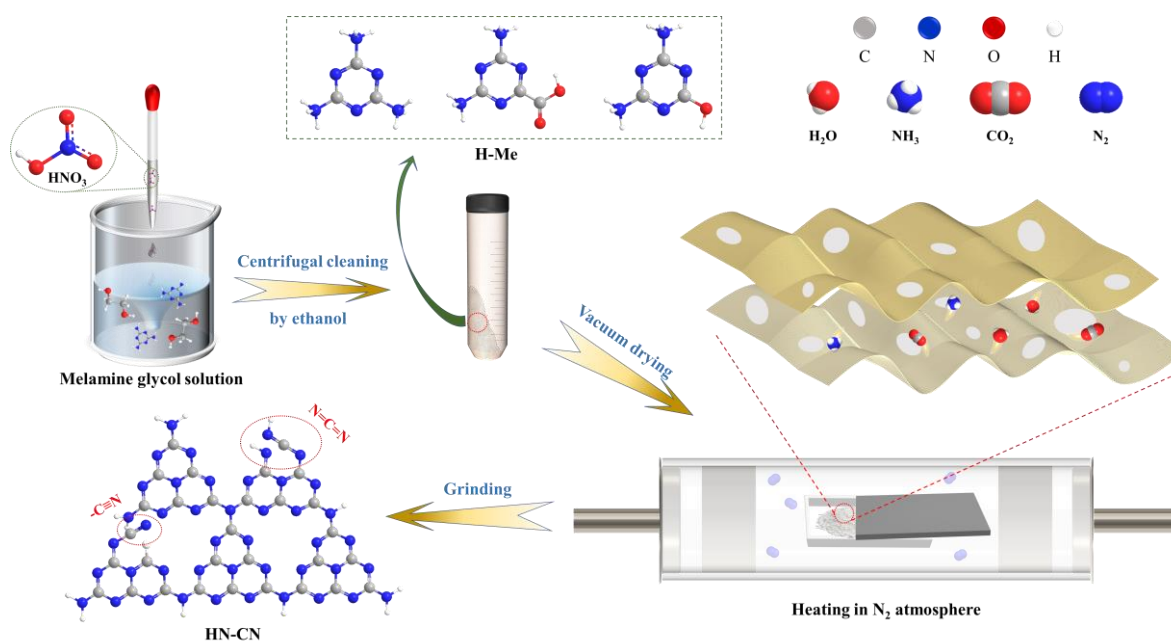


Figure 1. Schematic illustration of the preparation process of HN-CN.

The information on crystal and chemical structure was detected to identify the end product. In the XRD pattern (Figure 2a), all samples exhibit a strong diffraction peak near 27.45° , corresponding to the stacking of the (002) crystal plane of $g\text{-C}_3\text{N}_4$, namely, the graphite layer. The other characteristic peak of $g\text{-C}_3\text{N}_4$ is located near 13.2° , which corresponds to the (100) crystal plane, the in-plane repeat of the heptazine ring [24]. The intensity of both characteristic peaks of N-CN is slightly reduced compared to CN, and the diffraction peak corresponding to the (100) crystal plane is shifted to a lower angle of 12.9° , reflecting the greater distance among the heptazine rings. The reason for this phenomenon may be that the introduction of many defects disrupts the long-range ordering of the $g\text{-C}_3\text{N}_4$ structure. It should be observed that the samples (H-CN and HN-CN) developed from the protonated precursor exhibit similar and markedly weaker XRD signals, because the shock of abundant endogenous gas causes a more fragmented, porous, thin layer structure to emerge.

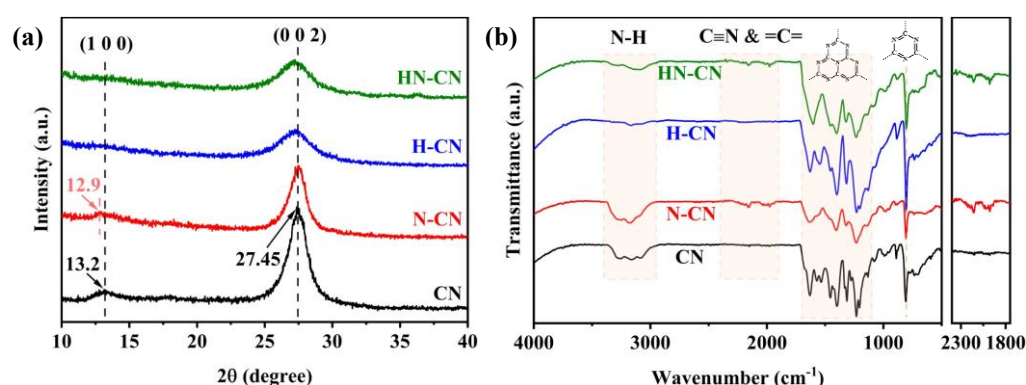


Figure 2. (a) XRD patterns and (b) FTIR spectra of CN, N-CN, H-CN, and HN-CN.

In FTIR spectra, all samples showed characteristic signals of $g\text{-C}_3\text{N}_4$ in the region of 804 cm^{-1} and $1200\text{--}1700\text{ cm}^{-1}$, corresponding to the respiration vibration of the triazine ring and the stretching vibration of the carbon-nitrogen heterocycle, respectively. In these two regions, the signal intensity of N-CN was significantly weaker compared to CN, while H-CN was significantly enhanced. Additionally, carefully comparing the $1200\text{--}1700\text{ cm}^{-1}$ region can reveal that N-CN and HN-CN have similar peak shapes as well as H-CN and CN. The above phenomenon reflects the effect of defects formation in N_2 atmosphere on the structure of conjugated heterocycles. The signal located in the $2900\text{--}3400\text{ cm}^{-1}$ region is attributed to the stretching vibration of the N-H bond in the -NH_2 groups [25], which come from the incomplete polymerization of melem, and will become a recombination site for photogenerated carriers to reduce the photocatalytic activity of $g\text{-C}_3\text{N}_4$. Due to a large quantity of defects, the -NH_2 groups signal of N-CN is significantly enhanced, and in contrast, the signal of HN-CN and H-CN is significantly attenuated, because the protonated precursor can be polymerized better during the subsequent heat treatment. Although the polymerization in N_2 atmosphere and the protonation treatment of the precursor both bring some effects on the structure of the prepared $g\text{-C}_3\text{N}_4$, similar XRD and FTIR patterns also indicate that the basic $g\text{-C}_3\text{N}_4$ framework is well preserved. Except for the standard $g\text{-C}_3\text{N}_4$ signal, some small peaks in the range of $1900\text{--}2400\text{ cm}^{-1}$ can be observed for the samples prepared in the N_2 atmosphere. This range belongs to carbon-nitrogen triple bond ($\text{C}\equiv\text{N}$) and accumulated double bonds ($=\text{C}=\text{C}$), which well reflects some types of defects in N-CN and HN-CN.

The specific surface area is one of the key factors affecting catalytic activity [26], since a greater specific surface area can expose more redox reaction active sites, shorten the photogenerated carrier transport distance, and maximize the utilization of visible light. In the N_2 adsorption–desorption isotherms (Figure 3a), all samples exhibited type IV isotherms and H3 hysteresis loops, indicating that the slit pores formed by the accumulation of lamellar particles are present in the prepared samples [27]. The BET-specific surface area

of each sample is also shown in Figure 3a, where it can be seen that the specific surface area of N-CN synthesized in N_2 atmosphere ($9.5 \text{ m}^2/\text{g}$) is marginally greater than that of CN synthesized in air atmosphere ($8.3 \text{ m}^2/\text{g}$), while the specific surface area of H-CN polymerized by protonated precursor ($20.6 \text{ m}^2/\text{g}$) is remarkably increased. For the BJH pore size distribution curve (Figure 3b), the vertical axis dV/dD is the pore volume per unit pore size in unit mass of sample (where V is the pore volume and D is the pore diameter). The increase in the specific surface area of N-CN is due to the increased volume of pores in the 10–30 nm diameter range, corresponding to the accumulation of broken small grains due to partial polymerization. While H-CN exhibits the maximum pore volume with diameters in the range of 2–5 nm, corresponding to the vents formed by endogenous gas release [28]. The vent content of HN-CN was also significantly increased, but it was still less than that of H-CN (specific surface area lower than HN-CN), indicating that the number of vents was not the main factor for the increase in specific surface areas. The significant increase in the specific surface area of the samples synthesized by a protonated precursor is mainly attributable to the formation of smaller and thinner nanosheets involved in the exfoliation of endogenous gas. HN-CN has the largest specific surface area ($28.7 \text{ m}^2/\text{g}$) and pore volume ($0.07 \text{ cm}^3/\text{g}$) as it has both reason of N-CN and H-CN to increase their specific surface area. The larger specific surface area and pore volume not only increases the reaction interface but also facilitates the reflection of incident photons within the pore channels to maximize the absorption of light energy to drive subsequent reactions.

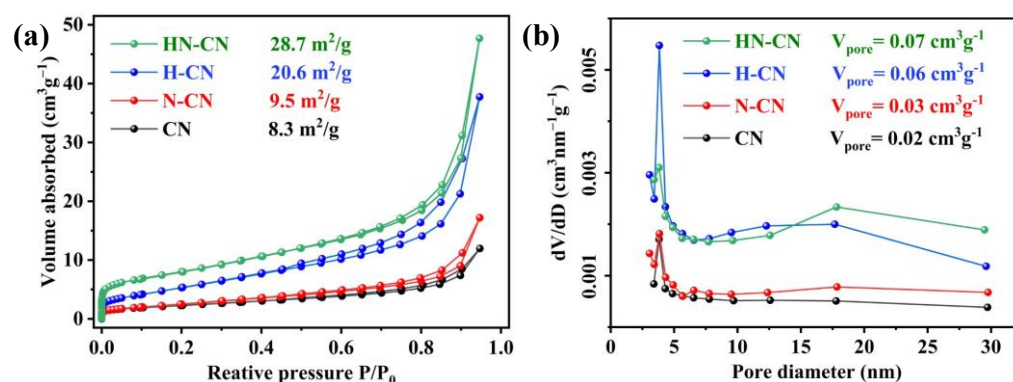


Figure 3. (a) N_2 adsorption–desorption isotherms and (b) pore size distribution curves of CN, N-CN, H-CN, and HN-CN.

The above conclusions were verified by microscopic images. In the SEM images (Figures 4a–d and S2), CN displays a conventional large bulk structure with a smooth surface, while N-CN shows a block made up of multiple compact bulks with a rough surface, where each block is composed of countless small and nearly fused grains. Both H-CN and HN-CN exhibit obvious sheet stacking structures, but there are more large fissures and holes in HN-CN. Similar results can be seen in the TEM images (Figures 4e–h and S3), where the surfaces of CN and H-CN (prepared in air) are visibly flatter than those of N-CN and HN-CN (prepared in N_2), similarly only H-CN and HN-CN (polymerized by protonated precursor) show pores in the sheets. Additionally, two characteristic diffraction rings of $g\text{-C}_3\text{N}_4$ are observed in the selected area electron diffraction (SAED) pattern corresponding to (100) and (002) crystal planes [22], which is consistent with the XRD results. Additionally, the EDS elemental mappings (Figure S4) substantiate the uniform distribution of C and N elements in HN-CN.

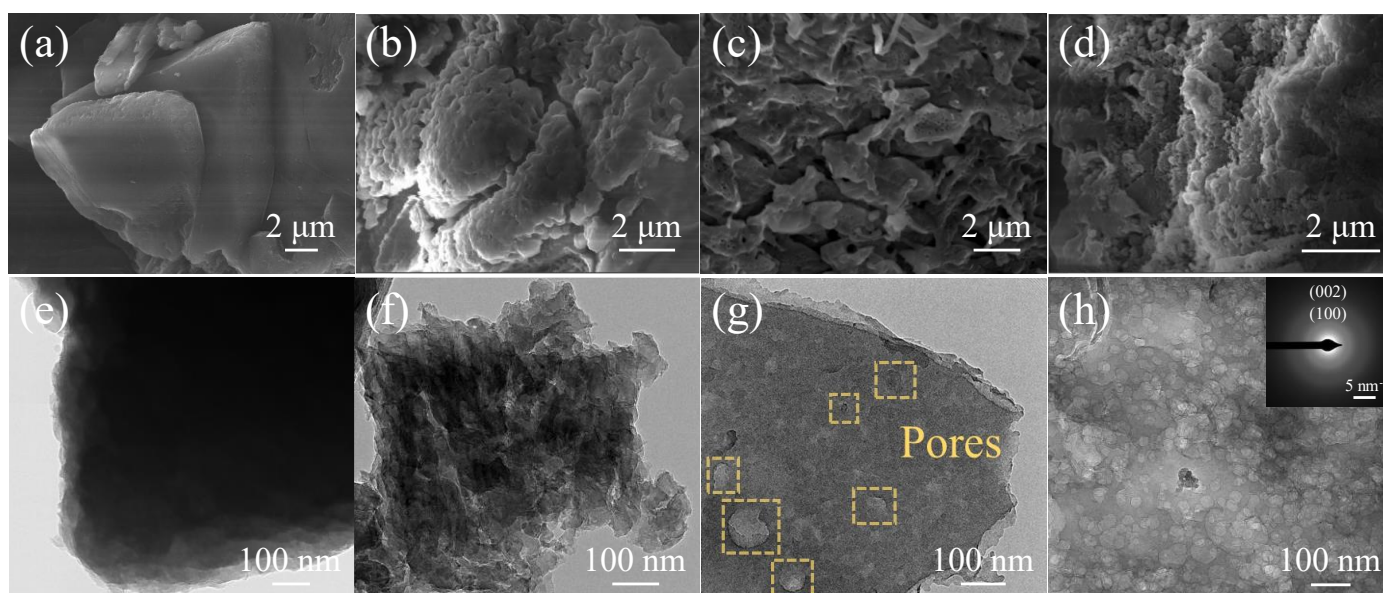


Figure 4. The SEM (above) and TEM (below) images of CN (a,e), N-CN (b,f), H-CN (c,g), and HN-CN (d,h).

The chemical environment of the samples was analyzed to recognize the structure of defects and deduce the formation reason for defects introduced by heat treatment of the protonated precursors in N_2 atmosphere. Elemental analysis (Table S1) shows that the prepared samples merely consisted of C, N, H, and O elements. The surface of all prepared samples contains C, N, and O elements according to the XPS survey spectrum (Figure S5), and only a single peak appears at the binding energy of 532 eV, referring to the high-resolution O 1s spectrum (Figure S6), aligning with surface-adsorbed water [29]. According to the facts presented above, this experiment did not introduce exotic atoms into the structure of $g-C_3N_4$.

For the high-resolution C1s spectra (Figure 5a), all samples can be divided into four peaks. The peak located at 284.6 eV corresponds to the adventitious graphitic carbon (C-C, denoted C1) and is used for binding energy correction. The signal near 286.1 eV comes from carbon in the $C-NH_x$ ($x = 1,2$) or $-C\equiv N$ structure (denoted as C2) because they have similar binding energies for C 1s [25,30,31]. The signal at about 287.9 eV is derived from the sp^2 -hybridized carbon in the $N=C(-N)-N$ structure (denoted as C3), and the signal near 288.9 eV is attributed to the carbon coordinated with two nitrogen atoms ($C(-N)_2$), denoted as C4) [14,16,20]. Further calculations of the proportion of different type carbons (Table S2) show clearly that the proportion of C4 increases violently from 6.8% for CN to 41.2% for N-CN, and the proportion of C3 decreases drastically from 76.4% for CN to 45.9% for N-CN, indicating that the part carbon that should be polymerized to the triple-coordinated carbon ($N=C(-N)-N$) as the framework of $g-C_3N_4$ is converted to two-coordinated carbon due to N_2 atmosphere. Combined with the appearance of signals at the accumulated double bond region in the FTIR spectrum, it indicates the presence of $N=C=N$ structure in the sample N-CN. Compared to CN, H-CN has a smaller C2 and C4 share and a noticeably greater C3 share, demonstrating an increase in polymerization, which is consistent with previous reports that protonation treatment of precursor can improve the polymerization of generated $g-C_3N_4$ [21]. It is noteworthy that the C4 share of HN-CN is not increased and the C3 share is increased compared to CN, so it can be speculated that the protonation treatment precursors can further polymerize the defects such as $=CH-NH_x$ ($x = 0, 1, 2$) to $N=C(-N)-N$.

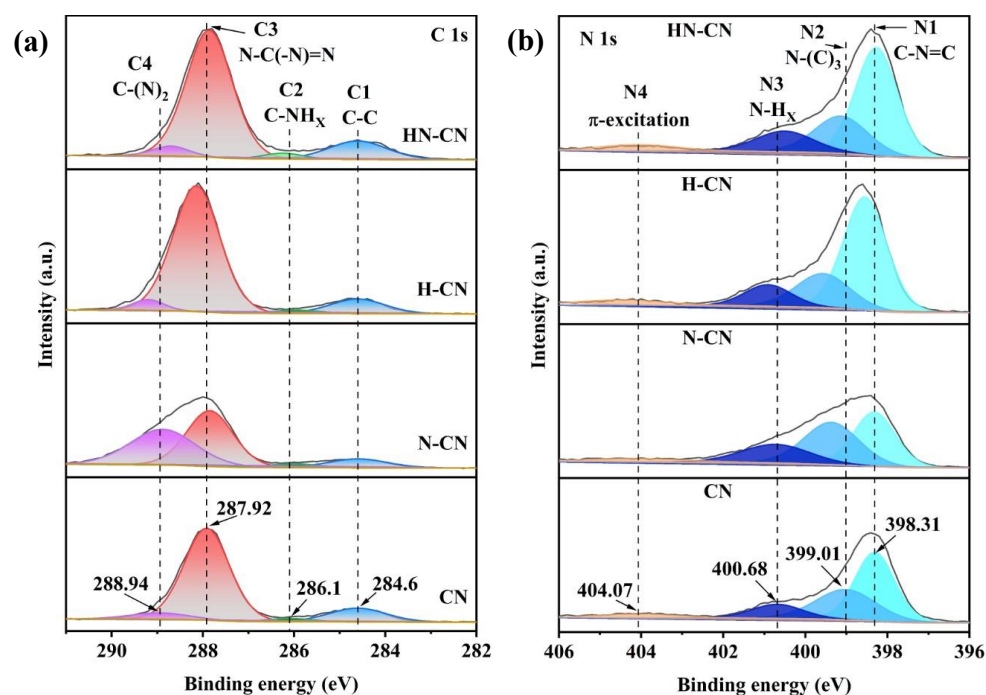


Figure 5. High-resolution XPS spectra of C 1s (a), N 1s (b) of CN, N-CN, H-CN, and HN-CN.

Next, looking at the high-resolution N 1s spectrum (Figure 5b), the four deconvoluted peaks located near 398.3 eV, 399.0 eV, 400.7 eV, and 404 eV originate from the sp^2 -hybridized nitrogen C-N=C (denoted as N1), the sp^3 -hybridized tertiary nitrogen N-(C)₃ (denoted as N2), the amino nitrogen (denoted as N3), and the π -excitation effect (denoted as N4), respectively [32–35]. In combination with the percentage of different types of nitrogen (Table S3) to analyze shows that the proportion of N1 in N-CN compared to CN is reduced but not N2, and the amino nitrogen (N3) increases. This indicates that the preparation of g-C₃N₄ in N₂ atmosphere mainly affects the formation of sp^2 -hybridized nitrogen in the framework of the heptazine ring, which is different from the results of heat treatment of already synthesized g-C₃N₄ in N₂ atmosphere [14]. Similarly, H-CN exhibited the top polymerization among all the prepared samples because it had the highest N1 and lowest N3 percentages. The value of (N1+N2)/N3 is commonly used to reflect the degree of nitrogen defects in g-C₃N₄ [20]. This value is 6.65 for H-CN is the maximum in all samples and corresponds to the least quantity of nitrogen defects, while the value falls in varying levels for the samples synthesized in the N₂ atmosphere (3.6 for N-CN and 5.47 for HN-CN), confirming the induction of nitrogen defects by N₂ atmosphere. Finally, HN-CN well combines the advantages of heat treatment in N₂ atmosphere and the protonation of the precursor, improving the degree of polymerization while retaining a moderate quantity of defects (e.g., -C≡N, N=C=N). As an addition here, it can be seen that in the C 1s and N 1s spectra of H-CN, all peaks are shifted to the direction of high binding energy, which is due to fewer defects and more interconnection of heptazine rings, resulting in a larger and more structurally complete graphite layer, thus increasing the overlap and expansion of π -orbital.

Through a comprehensive analysis of the above conclusions, the synthetic route and the ultimate chemical structure of each sample could be supposed. Firstly, we analyze the effect of N₂ atmosphere on the synthesis of g-C₃N₄ (Figure 6): it is well known that in the classical synthetic pathway, with the temperature rise, melamine (I) will first combine two by two to melam (II), then synthesize to melem (V), further condense to melom (VI), and finally produce the ideal g-C₃N₄ [36]. However, the g-C₃N₄ synthesized in N₂ atmosphere appears the disruption of the C-N=C and N=C(-N)-N structure in the heptazine ring, so it can be speculated that the defects introduced by N₂ atmosphere are formed during the transition from melam (II) to melem (V). Considering that N₂ is very stable chemically

3.2. Optical and Carrier Properties

The band gap is determined by the light absorption capacity of the samples. As seen in the UV-vis diffuse reflectance spectra (DRS) (Figure 8a), the samples synthesized in the N_2 atmosphere exhibit significantly enhanced visible absorption in the >440 nm range, which is triggered by the $n \rightarrow \pi^*$ transition of the lone-pair electrons at the defect sites [37,38]. Moreover, the apparent light absorption at <400 nm for all samples stems from the intrinsic absorption of $g\text{-C}_3\text{N}_4$ generated by $\pi \rightarrow \pi^*$ transition of electrons. In that there are no additional chemical and electronic structure optimizations and only an increase in the polymerization and specific surface area, there is no significant change in the light absorption of H-CN, rather there is a slight enhancement in intrinsic absorption caused by the overlap and expansion of π -orbitals (in line with the XPS conclusion). The light absorption of HN-CN is significantly enhanced in the full spectral range compared to N-CN because the larger specific surface area and more pore channels allow HN-CN to expose more interfaces to absorb light energy, and the transition of electrons in N-CN is suppressed due to the defects of complex types restricting each other. Therefore, with the modulation of moderate and suitable defects, HN-CN has the best light absorption ability among all samples, which provides a good guarantee for photocatalytic activity.

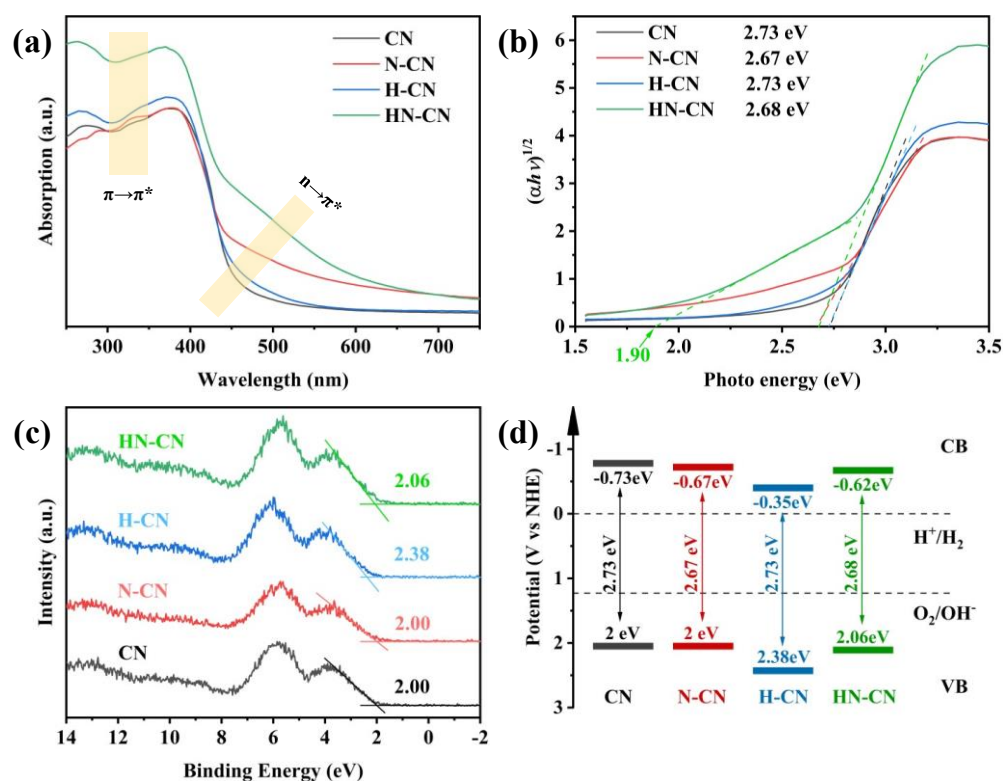


Figure 8. (a) UV–Vis DRS spectra, (b) plots of converted Kubelka–Munk functions vs. photon energy, (c) XPS VB spectra, and (d) corresponding electronic band structures of CN, N-CN, H-CN, and HN-CN.

The band gap of the samples was calculated by the transformed Kubelka–Munk function (Figure 8b), and the results showed that CN and H-CN have an approximately equal band gap (2.73 eV), indicating that an appropriate increase in the polymerization does not alter the intrinsic band gap of $g\text{-C}_3\text{N}_4$. In contrast, N-CN (2.67 eV) and HN-CN (2.68 eV) have similarly narrowed band gaps, reflecting the modulation effect of the defects on the electronic structure. Furthermore, a mid-gap (1.9 eV) can be easily observed in HN-CN, which enables more electrons to be excited by visible light. The valence band information of the samples was measured using XPS (Figure 8c). After simple processing, we can discover that CN, N-CN, and HN-CN have similar valence band positions (2 eV,

2 eV, and 2.06 eV, respectively), while that of H-CN is positively shifted to 2.38 eV due to a more long-range order of the electronic state. The energy band structure of all samples was schematically drawn based on the above information (Figure 8d). It can be seen that the effect of the defects induced by the N₂ atmosphere on the electronic structure of the samples was mainly focused on the conduction band. Moreover, although there is a slight downward shift of the band gap, HN-CN well inherits the narrowed band gap due to the introduction of defects, while maintaining a high conduction band position to ensure the reduction ability of photogenerated electrons.

The PL spectra of the samples were tested since defects can significantly affect the separation ability of photogenerated carriers (Figure 9a). With the elimination of the unfavorable defects, HN-CN exhibits a very low fluorescence intensity, which is the reason for the promoting exciton dissociation by accumulated double bonds and -C≡N groups, and the facilitating migration of photogenerated carriers by the increased polymerization. In contrast, N-CN exhibits the highest fluorescence radiation intensity, which may be due to the rapid recombination of photogenerated carriers at unfavorable defects (e.g., -NH₂ groups). To characterize the density and transport capacity of photogenerated carriers, a series of electrochemical tests are performed on the samples [39,40]. The electrochemical impedance spectroscopy (EIS) of the samples (Figure 9b) show that N-CN exhibits the largest arc radius, i.e., the highest charge transport resistance (R_{ct}), which is owing to carrier transfer hindered by a mass of defects. The R_{ct} of HN-CN and H-CN is distinctly lower due to the increase of polymerization, where H-CN has lower resistance because of fewer defects. A roughly similar phenomenon is shown in the transient photocurrent response curves (Figure 9c), where HN-CN and H-CN have significantly enhanced photocurrent intensities, but that of HN-CN is higher. This is because the photocurrent intensity is related to the density and transfer rate of photogenerated carriers, which also indicates that HN-CN has more photogenerated carriers than H-CN.

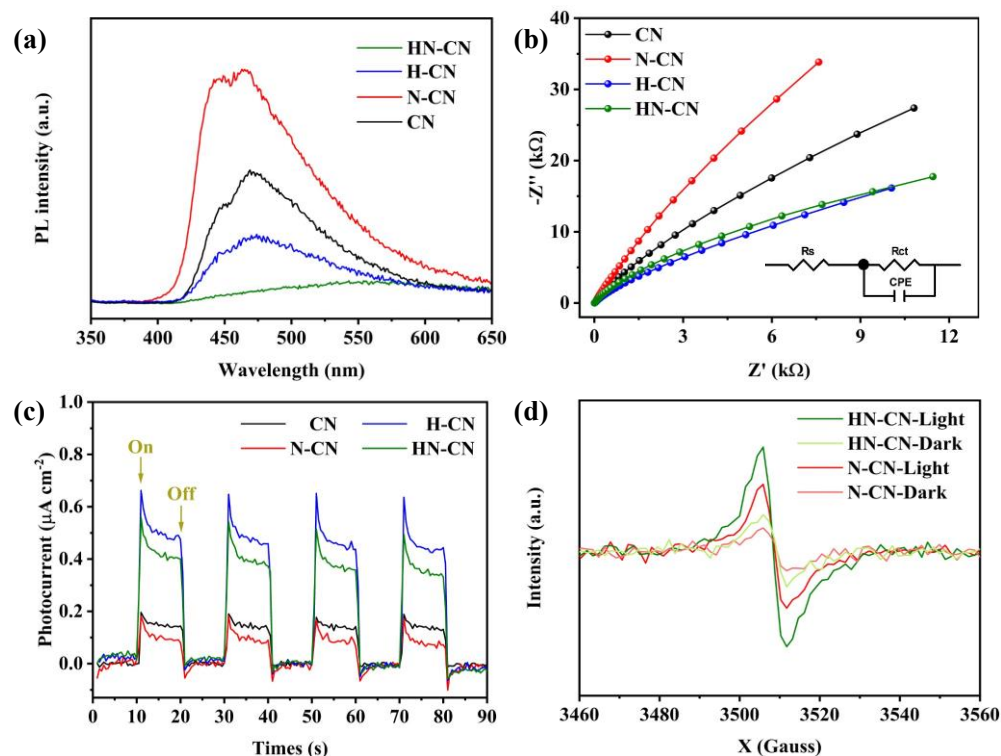


Figure 9. (a) Steady-state PL spectra, (b) EIS Nyquist plots, and (c) transient photocurrent response of CN, N-CN, H-CN, and HN-CN, (d) EPR spectra of N-CN and HN-CN.

The increase in carrier density originates from the modulation of defects to the electronic structure. To investigate whether HN-CN retains only the defects contributing to

increase carrier density, the EPR spectra and Mott-Schottky curves were used to compare the carrier density of the samples prepared in N_2 atmosphere. According to the Lorentz single peaks at the same position in Figure 9d, the sp^2 -hybridized carbon atoms in both N-CN and HN-CN generated the same type of unpaired electrons [41]. However, the Lorentz curve of HN-CN exhibits higher intensity in both visible light and dark conditions, reflecting higher delocalized electron density. Mott-Schottky curves (Figure S7b) can be used to determine the type of semiconductor, obtain the flat-band potential of the material, and reflect the density of the majority carrier in the sample [42]. The positive slope indicates that both N-CN and HN-CN are typical n-type semiconductors, and further calculation of the inverse of the slope shows that the carrier density of HN-CN is 1.14 times higher than that of N-CN. This result is good evidence that the step of protonated precursor can remove the defects generated in the N_2 atmosphere that are detrimental to the carrier density increase. Moreover, the intercept of the tangent line to the transverse axis is in line with the flat-band potential of the samples, and the similar flat-band potential suggests that they have close conduction band potential, which is consistent with Figure 8d.

3.3. Photocatalytic H_2 Evolution Performance

Due to the much greater specific surface area, higher polymerization, improved electronic structure, good visible-light absorption, electron transport capabilities, and increased carrier density, HN-CN has outstanding photocatalytic hydrogen evolution performance (Figure 10a). We further calculated the hydrogen evolution rate (HER) for each sample (Figure 10b), where the HER of HN-CN reached $675.5 \mu\text{mol}\cdot\text{h}^{-1}\cdot\text{g}^{-1}$ which was 7.5 times higher than that of N-CN ($89.9 \mu\text{mol}\cdot\text{h}^{-1}\cdot\text{g}^{-1}$) and 4.1 times higher than that of CN ($164.5 \mu\text{mol}\cdot\text{h}^{-1}\cdot\text{g}^{-1}$). This indicates that the hydrogen evolution activity can be significantly improved by controlling the quantity and type of defects in $g\text{-C}_3\text{N}_4$ polymerized in N_2 atmosphere. For excluding the effect of specific surface area on performance enhancement, the HER per surface area (HERs) was also calculated (Figure 10b). It can be seen that the HERs of HN-CN is still higher than that of CN and H-CN, reflecting the important role of the defects retained in HN-CN in regulating the electronic structure and enhancing the performance of photocatalytic hydrogen evolution.

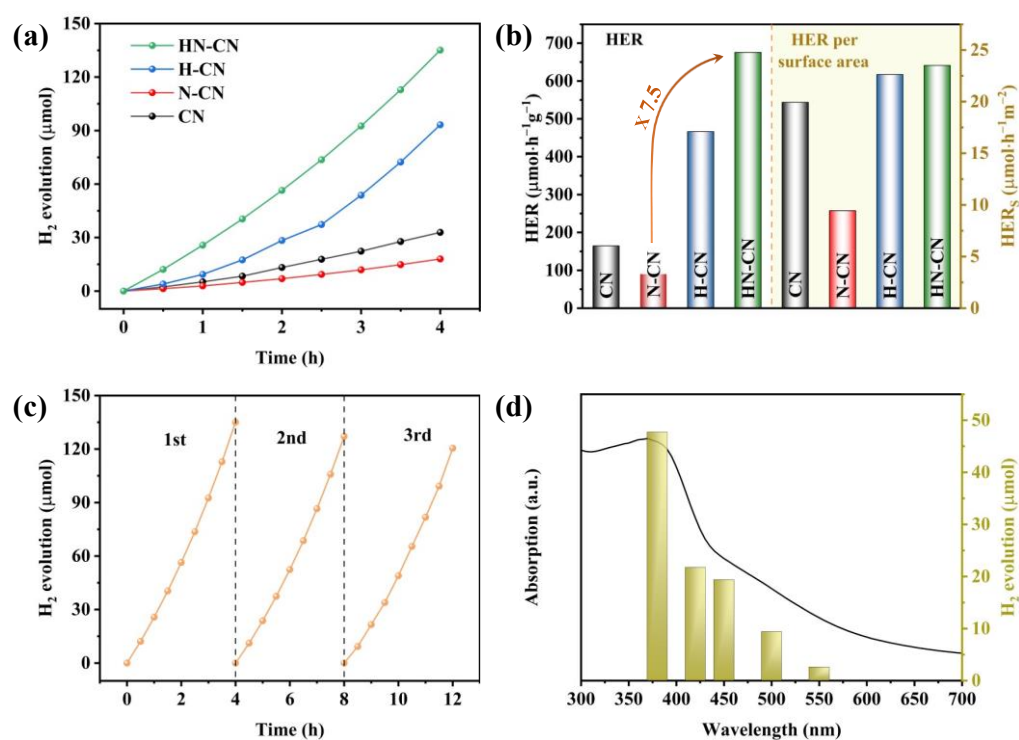


Figure 10. (a) Temporal evolution of the H_2 evolution curves and (b) HER of CN, N-CN, H-CN, and HN-CN. (c) Stability test and (d) wavelength-dependent of the H_2 evolution of HN-CN.

The stability of HN-CN was verified by photocatalytic cycling experiments (Figure 10c). After three cycles of tests, there was no significant decrease in hydrogen evolution activity, which proved that HN-CN has good resistance to water and photo-corrosion. To verify that the photocatalytic water splitting reaction is driven by the absorption of incident photons, the hydrogen evolution performance of HN-CN at different wavelengths was tested (Figure 10d). The results show that the tendency of H₂ evolution matches well with the light absorption of HN-CN, indicating the H₂ derived from the reduction of H⁺ by electrons excited by the energy band.

4. Conclusions

This work focuses on the effect of N₂ atmosphere on the synthesis of g-C₃N₄. We propose that when calcining the nitrogen-rich precursor of g-C₃N₄ in N₂ atmosphere, the melam to melem transition is restricted due to a lack of O₂ assistance, which leads to a substantial quantity of defects in the synthesized g-C₃N₄. To enhance its photocatalytic property, we propose a method to reduce the quantity of defects due to calcinating in N₂ atmosphere by protonating the precursor in a way that increases the polymerization of the product. Meanwhile, protonated melamine can release a large amount of endogenous gas during the thermal polycondensation process, and the endogenous gas can in-situ exfoliate the graphite layer of g-C₃N₄, resulting in a significant increase in the specific surface area of the product. The results show that only a moderate quantity of defects (e.g., -C≡N, N=C=N) that contribute to electron excitation and enhance the separation efficiency and density of photogenerated carriers were retained under the synergistic effect of N₂ atmosphere and protonation. Ultimately, HN-CN exhibited excellent photocatalytic hydrogen evolution performance, which was 7.5 times higher than that of N-CN prepared in N₂ atmosphere. This work not only provides a fresh perspective on how to introduce the right quantity of defects, but also provides a deeper opinion on the intrinsic mechanism of defects formation in N₂ atmosphere.

Supplementary Materials: The following supporting information can be downloaded at: <https://www.mdpi.com/article/10.3390/catal13020269/s1>, Figure S1: The weight of CN (a), N-CN (b), H-CN (c), and HN-CN (d), and their volume comparison (e); Figure S2: SEM images of CN (a) (b), H-CN (c) (d), N-CN (e) (f), and HN-CN (g) (h); Figure S3: TEM images of CN (a), H-CN (b), N-CN (c) (d), and HN-CN (e) (f). Inset in (f) is the SAED pattern; Figure S4: EDS elemental mapping patterns of HN-CN; Figure S5: XPS survey spectrum of CN (a), N-CN (b), H-CN (c), and HN-CN (d); Figure S6: High resolution XPS O 1s spectra of CN, N-CN, H-CN, and HN-CN; Figure S7: (a) EPR g-factor and (b) Mott-Schottky curves of N-CN and HN-CN; Table S1: The elemental analysis of different samples: CN, N-CN, H-CN, and HN-CN; Table S2: The fractions of various C types for different samples: CN, N-CN, H-CN, and HN-CN; Table S3: The fractions of various N types for different samples: CN, N-CN, H-CN, and HN-CN.

Author Contributions: X.C.: Conceptualization, Investigation, Data Curation, Formal analysis, Writing—Original Draft; H.F.: Resources, Supervision, Funding acquisition; L.L.: Writing—Review and Editing; X.W.: Writing—Review and Editing; L.M.: Writing—Review and Editing, Funding acquisition; W.W.: Writing—Review and Editing, Funding acquisition. All authors have read and agreed to the published version of the manuscript.

Funding: This research was funded by the National Key Research and Development Project (2020YFC1521900 and 2020YFC1521904), the Shaanxi Provincial Science Foundation (2021GXLH-01-11), the National Natural Science Foundation of China (51902259), the SKLSP Project (2019-TZ-04), and the 111 Program (B08040) of MOE. This work was also supported by the Fundamental Research Funds for the Central Universities (0515022GH0202253 and 0515022SH0201253), National Natural Science Foundation of China (52202299) and the Analytical & Testing Center of Northwestern Polytechnical University (2022T006).

Data Availability Statement: Not applicable.

Acknowledgments: We would also like to thank the Analysis & Testing Center of NPU for providing the testing conditions.

Conflicts of Interest: The authors declare no conflict of interest.

References

1. Liao, C.-H.; Huang, C.-W.; Wu, J.C.S. Hydrogen Production from Semiconductor-based Photocatalysis via Water Splitting. *Catalysts* **2012**, *2*, 490–516. [[CrossRef](#)]
2. Ong, W.-J.; Tan, L.-L.; Ng, Y.H.; Yong, S.-T.; Chai, S.-P. Graphitic Carbon Nitride (g-C₃N₄)-Based Photocatalysts for Artificial Photosynthesis and Environmental Remediation: Are We a Step Closer to Achieving Sustainability? *Chem. Rev.* **2016**, *116*, 7159–7329. [[CrossRef](#)] [[PubMed](#)]
3. Li, L.; Hasan, I.M.U.; Farwa; He, R.; Peng, L.; Xu, N.; Niazi, N.K.; Zhang, J.-N.; Qiao, J. Copper as a single metal atom based photo-, electro-, and photoelectrochemical catalyst decorated on carbon nitride surface for efficient CO₂ reduction: A review. *Nano Res. Energy* **2022**, *1*, e9120015. [[CrossRef](#)]
4. Yu, Y.; Huang, H. Coupled adsorption and photocatalysis of g-C₃N₄ based composites: Material synthesis, mechanism, and environmental applications. *Chem. Eng. J.* **2023**, *453*, 139755. [[CrossRef](#)]
5. Lin, H.; Wu, J.; Zhou, F.; Zhao, X.; Lu, P.; Sun, G.; Song, Y.; Li, Y.; Liu, X.; Dai, H. Graphitic carbon nitride-based photocatalysts in the applications of environmental catalysis. *J. Environ. Sci.* **2023**, *124*, 570–590. [[CrossRef](#)] [[PubMed](#)]
6. Tang, C.; Cheng, M.; Lai, C.; Li, L.; Yang, X.; Du, L.; Zhang, G.; Wang, G.; Yang, L. Recent progress in the applications of non-metal modified graphitic carbon nitride in photocatalysis. *Coord. Chem. Rev.* **2023**, *474*, 214846. [[CrossRef](#)]
7. Tay, Q.; Kanhere, P.; Ng, C.F.; Chen, S.; Chakraborty, S.; Huan, A.C.H.; Sum, T.C.; Ahuja, R.; Chen, Z. Defect Engineered g-C₃N₄ for Efficient Visible Light Photocatalytic Hydrogen Production. *Chem. Mater.* **2015**, *27*, 4930–4933. [[CrossRef](#)]
8. Yu, H.; Shi, R.; Zhao, Y.; Bian, T.; Zhao, Y.; Zhou, C.; Waterhouse, G.I.N.; Wu, L.-Z.; Tung, C.-H.; Zhang, T. Alkali-Assisted Synthesis of Nitrogen Deficient Graphitic Carbon Nitride with Tunable Band Structures for Efficient Visible-Light-Driven Hydrogen Evolution. *Adv. Mater.* **2017**, *29*, 1605148. [[CrossRef](#)]
9. Shi, L.; Yang, L.; Zhou, W.; Liu, Y.; Yin, L.; Hai, X.; Song, H.; Ye, J. Photoassisted Construction of Holey Defective g-C₃N₄ Photocatalysts for Efficient Visible-Light-Driven H₂O₂ Production. *Small* **2018**, *14*, 1703142. [[CrossRef](#)]
10. Lan, H.; Li, L.; An, X.; Liu, F.; Chen, C.; Liu, H.; Qu, J. Microstructure of carbon nitride affecting synergetic photocatalytic activity: Hydrogen bonds vs. structural defects. *Appl. Catal. B-Environ.* **2017**, *204*, 49–57. [[CrossRef](#)]
11. Lau, V.W.-H.; Yu, V.W.-Z.; Ehrat, F.; Botari, T.; Moudrakovski, I.; Simon, T.; Duppel, V.; Medina, E.; Stolarczyk, J.K.; Feldmann, J.; et al. Urea-Modified Carbon Nitrides: Enhancing Photocatalytic Hydrogen Evolution by Rational Defect Engineering. *Adv. Energy Mater.* **2017**, *7*, 1602251. [[CrossRef](#)]
12. Wang, K.; Fu, J.; Zheng, Y. Insights into photocatalytic CO₂ reduction on C₃N₄: Strategy of simultaneous B, K co-doping and enhancement by N vacancies. *Appl. Catal. B-Environ.* **2019**, *254*, 270–282. [[CrossRef](#)]
13. Huang, Z.-F.; Song, J.; Pan, L.; Wang, Z.; Zhang, X.; Zou, J.-J.; Mi, W.; Zhang, X.; Wang, L. Carbon nitride with simultaneous porous network and O-doping for efficient solar-energy-driven hydrogen evolution. *Nano Energy* **2015**, *12*, 646–656. [[CrossRef](#)]
14. Dong, G.; Ho, W.; Wang, C. Selective photocatalytic N₂ fixation dependent on g-C₃N₄ induced by nitrogen vacancies. *J. Mater. Chem. A* **2015**, *3*, 23435–23441. [[CrossRef](#)]
15. Wang, Y.; Meng, D.; Zhao, X. Visible-light-driven H₂O₂ production from O₂ reduction with nitrogen vacancy-rich and porous graphitic carbon nitride. *Appl. Catal. B-Environ.* **2020**, *273*, 119064. [[CrossRef](#)]
16. Li, X.; Hartley, G.; Ward, A.J.; Young, P.A.; Masters, A.F.; Maschmeyer, T. Hydrogenated Defects in Graphitic Carbon Nitride Nanosheets for Improved Photocatalytic Hydrogen Evolution. *J. Phys. Chem. C* **2015**, *119*, 14938–14946. [[CrossRef](#)]
17. Yang, S.; Gong, Y.; Zhang, J.; Zhan, L.; Ma, L.; Fang, Z.; Vajtai, R.; Wang, X.; Ajayan, P.M. Exfoliated Graphitic Carbon Nitride Nanosheets as Efficient Catalysts for Hydrogen Evolution Under Visible Light. *Adv. Mater.* **2013**, *25*, 2452–2456. [[CrossRef](#)]
18. Yin, Y.; Han, J.; Zhang, X.; Zhang, Y.; Zhou, J.; Muir, D.; Sutarro, R.; Zhang, Z.; Liu, S.; Song, B. Facile synthesis of few-layer-thick carbon nitride nanosheets by liquid ammonia-assisted lithiation method and their photocatalytic redox properties. *Rsc Adv.* **2014**, *4*, 32690–32697. [[CrossRef](#)]
19. Niu, P.; Zhang, L.; Liu, G.; Cheng, H.-M. Graphene-Like Carbon Nitride Nanosheets for Improved Photocatalytic Activities. *Adv. Funct. Mater.* **2012**, *22*, 4763–4770. [[CrossRef](#)]
20. Gao, S.; Wang, X.; Song, C.; Zhou, S.; Yang, F.; Kong, Y. Engineering carbon-defects on ultrathin g-C₃N₄ allows one-pot output and dramatically boosts photoredox catalytic activity. *Appl. Catal. B-Environ.* **2021**, *295*, 120272. [[CrossRef](#)]
21. Zhong, Y.; Wang, Z.; Feng, J.; Yan, S.; Zhang, H.; Li, Z.; Zou, Z. Improvement in photocatalytic H₂ evolution over g-C₃N₄ prepared from protonated melamine. *Appl. Surf. Sci.* **2014**, *295*, 253–259. [[CrossRef](#)]
22. Lei, L.; Wang, W.; Shang, Y.; Li, J.; Yadav, A.K.; Wang, H.; Li, Q.; Fan, H. Tailoring chemical structures and intermolecular interactions of melem intermediates for highly efficient photocatalytic hydrogen evolution of g-C₃N₄. *Appl. Surf. Sci.* **2021**, *563*, 150384. [[CrossRef](#)]
23. Tahir, M.; Cao, C.; Butt, F.K.; Idrees, F.; Mahmood, N.; Ali, Z.; Aslam, I.; Tanveer, M.; Rizwan, M.; Mahmood, T. Tubular graphitic-C₃N₄: A prospective material for energy storage and green photocatalysis. *J. Mater. Chem. A* **2013**, *1*, 13949–13955. [[CrossRef](#)]
24. Guo, S.; Deng, Z.; Li, M.; Jiang, B.; Tian, C.; Pan, Q.; Fu, H. Phosphorus-Doped Carbon Nitride Tubes with a Layered Micro-nanostructure for Enhanced Visible-Light Photocatalytic Hydrogen Evolution. *Angew. Chem. Int. Edit.* **2016**, *55*, 1830–1834. [[CrossRef](#)]
25. Zhang, X.; Ma, P.; Wang, C.; Gan, L.; Chen, X.; Zhang, P.; Wang, Y.; Li, H.; Wang, L.; Zhou, X.; et al. Unraveling the dual defect sites in graphite carbon nitride for ultra-high photocatalytic H₂O₂ evolution. *Energy Environ. Sci.* **2022**, *15*, 830–842. [[CrossRef](#)]

26. Gu, J.; Peng, Y.; Zhou, T.; Ma, J.; Pang, H.; Yamauchi, Y. Porphyrin-based framework materials for energy conversion. *Nano Res. Energy* **2022**, *1*, e9120009. [[CrossRef](#)]
27. Hu, S.; Li, F.; Fan, Z.; Wang, F.; Zhao, Y.; Lv, Z. Band gap-tunable potassium doped graphitic carbon nitride with enhanced mineralization ability. *Dalton Trans.* **2015**, *44*, 1084–1092. [[CrossRef](#)] [[PubMed](#)]
28. Dong, G.; Wen, Y.; Fan, H.; Wang, C.; Cheng, Z.; Zhang, M.; Ma, J.; Zhang, S. Graphitic carbon nitride with thermally-induced nitrogen defects: An efficient process to enhance photocatalytic H₂ production performance. *Rsc Adv.* **2020**, *10*, 18632–18638. [[CrossRef](#)]
29. Li, K.; Su, F.-Y.; Zhang, W.-D. Modification of g-C₃N₄ nanosheets by carbon quantum dots for highly efficient photocatalytic generation of hydrogen. *Appl. Surf. Sci.* **2016**, *375*, 110–117. [[CrossRef](#)]
30. Wang, W.; Zhang, H.; Zhang, S.; Liu, Y.; Wang, G.; Sun, C.; Zhao, H. Potassium Ion Assisted Regeneration of Active Cyano Groups in Carbon Nitride Nanoribbons: Visible Light Driven Photocatalytic Nitrogen Reduction. *Angew. Chem. Int. Edit.* **2019**, *58*, 16644–16650. [[CrossRef](#)] [[PubMed](#)]
31. Wang, Y.; Du, P.; Pan, H.; Fu, L.; Zhang, Y.; Chen, J.; Du, Y.; Tang, N.; Liu, G. Increasing Solar Absorption of Atomically Thin 2D Carbon Nitride Sheets for Enhanced Visible-Light Photocatalysis. *Adv. Mater.* **2019**, *31*, 1807540. [[CrossRef](#)] [[PubMed](#)]
32. Zhao, S.; Zhang, Y.; Zhou, Y.; Wang, Y.; Qiu, K.; Zhang, C.; Fang, J.; Sheng, X. Facile one-step synthesis of hollow mesoporous g-C₃N₄ spheres with ultrathin nanosheets for photoredox water splitting. *Carbon* **2018**, *126*, 247–256. [[CrossRef](#)]
33. Li, Y.; Wang, S.; Chang, W.; Zhang, L.; Wu, Z.; Jin, R.; Xing, Y. Co-monomer engineering optimized electron delocalization system in carbon-bridging modified g-C₃N₄ nanosheets with efficient visible-light photocatalytic performance. *Appl. Catal. B-Environ.* **2020**, *274*, 119116. [[CrossRef](#)]
34. Giannakoudakis, D.A.; Seredych, M.; Rodríguez-Castellón, E.; Bandoz, T.J. Mesoporous Graphitic Carbon Nitride-Based Nanospheres as Visible-Light Active Chemical Warfare Agents Decontaminant. *ChemNanoMat* **2016**, *2*, 268–272. [[CrossRef](#)]
35. Seredych, M.; Los, S.; Giannakoudakis, D.A.; Rodríguez-Castellón, E.; Bandoz, T.J. Photoactivity of g-C₃N₄/S-Doped Porous Carbon Composite: Synergistic Effect of Composite Formation. *ChemSusChem* **2016**, *9*, 795–799. [[CrossRef](#)]
36. Thomas, A.; Fischer, A.; Goettmann, F.; Antonietti, M.; Mueller, J.-O.; Schloegl, R.; Carlsson, J.M. Graphitic carbon nitride materials: Variation of structure and morphology and their use as metal-free catalysts. *J. Mater. Chem.* **2008**, *18*, 4893–4908. [[CrossRef](#)]
37. Chen, Y.; Wang, B.; Lin, S.; Zhang, Y.; Wang, X. Activation of n→π* Transitions in Two-Dimensional Conjugated Polymers for Visible Light Photocatalysis. *J. Phys. Chem. C* **2014**, *118*, 29981–29989. [[CrossRef](#)]
38. Zhang, G.; Savateev, A.; Zhao, Y.; Li, L.; Antonietti, M. Advancing the n→π* electron transition of carbon nitride nanotubes for H₂ photosynthesis. *J. Mater. Chem. A* **2017**, *5*, 12723–12728. [[CrossRef](#)]
39. Chen, S.; Ma, L.; Huang, Z.; Liang, G.; Zhi, C. In situ/operando analysis of surface reconstruction of transition metal-based oxygen evolution electrocatalysts. *Cell Rep. Phys. Sci.* **2022**, *3*, 100729. [[CrossRef](#)]
40. Ma, L.; Ying, Y.; Chen, S.; Huang, Z.; Li, X.; Huang, H.; Zhi, C. Electrocatalytic Iodine Reduction Reaction Enabled by Aqueous Zinc-Iodine Battery with Improved Power and Energy Densities. *Angew. Chem. Int. Ed. Engl.* **2021**, *60*, 3791–3798. [[CrossRef](#)]
41. Yang, C.; Wang, B.; Zhang, L.; Yin, L.; Wang, X. Synthesis of Layered Carbonitrides from Biotic Molecules for Photoredox Transformations. *Angew. Chem. Int. Edit.* **2017**, *56*, 6627–6631. [[CrossRef](#)] [[PubMed](#)]
42. Fattah-alhosseini, A. Passivity of AISI 321 stainless steel in 0.5 M H₂SO₄ solution studied by Mott-Schottky analysis in conjunction with the point defect model. *Arab. J. Chem.* **2016**, *9*, S1342–S1348. [[CrossRef](#)]

Disclaimer/Publisher’s Note: The statements, opinions and data contained in all publications are solely those of the individual author(s) and contributor(s) and not of MDPI and/or the editor(s). MDPI and/or the editor(s) disclaim responsibility for any injury to people or property resulting from any ideas, methods, instructions or products referred to in the content.